The Meteoritical Society

Meteoritics & Planetary Science 50, Nr 8, 1338–1361 (2015)
doi: 10.1111/maps.12468

Nonporphyritic chondrules and chondrule fragments in enstatite chondrites: Insights into their origin and secondary processing

M. E. VARELA[1*], P. SYLVESTER[2,5], F. BRANDSTÄTTER[3], and A. ENGLER[4,6]

[1]Instituto de Ciencias Astronómicas de la Tierra y del Espacio (ICATE), Av. España 1512 sur, J5402DSP San Juan, Argentina
[2]Department of Earth Sciences, Memorial University of Newfoundland, St. John's, Newfoundland A1B 3X5, Canada
[3]Mineralogisch-Petrographische Abteilung, Naturhistorisches Museum, Burgring 7, 1010 Wien, Austria
[4]Institute of Earth Sciences, Department of Mineralogy and Petrology, University of Graz, 8010 Graz, Austria
[5]Present address: Department of Geosciences, Texas Tech University, Lubbock, Texas 79409–1053, USA
[6]Present address: Mariatrosterstrasse 305, 8044 Graz, Austria
[*]Corresponding author. E-mail: evarela@icate-conicet.gob.ar

(Received 27 October 2014; revision accepted 23 April 2015)

Abstract–Sixteen nonporphyritic chondrules and chondrule fragments were studied in polished thin and thick sections in two enstatite chondrites (ECs): twelve objects from unequilibrated EH3 Sahara 97158 and four objects from equilibrated EH4 Indarch. Bulk major element analyses, obtained with electron microprobe analysis (EMPA) and analytical scanning electron microscopy (ASEM), as well as bulk lithophile trace element analyses, determined by laser ablation inductively coupled plasma–mass spectrometry (LA-ICP-MS), show that volatile components (K_2O + Na_2O versus Al_2O_3) scatter roughly around the CI line, indicating equilibration with the chondritic reservoir. All lithophile trace element abundances in the chondrules from Sahara 97158 and Indarch are within the range of previous analyses of nonporphyritic chondrules in unequilibrated ordinary chondrites (UOCs). The unfractionated (solar-like) Yb/Ce ratio of the studied objects and the mostly unfractionated refractory lithophile trace element (RLTE) abundance patterns indicate an origin by direct condensation. However, the objects possess subchondritic CaO/Al_2O_3 ratios; superchondritic (Sahara 97158) and subchondritic (Indarch) Yb/Sc ratios; and chondritic-normalized deficits in Nb, Ti, V, and Mn relative to RLTEs. This suggests a unique nebular process for the origin of these ECs, involving elemental fractionation of the solar gas by the removal of oldhamite, niningerite, and/or another phase prior to chondrule condensation. A layered chondrule in Sahara 97158 is strongly depleted in Nb in the core compared to the rim, suggesting that the solar gas was heterogeneous on the time scales of chondrule formation. Late stage metasomatic events produced the compositional diversity of the studied objects by addition of moderately volatile and volatile elements. In the equilibrated Indarch chondrules, this late process has been further disturbed, possibly by a postaccretional process (diffusion?) that preferentially mobilized Rb with respect to Cs in the studied objects.

INTRODUCTION

Enstatite chondrites (ECs) comprise an inhomogeneous and scarce (<2% of the falls) group of meteorites with highly variable Fe and S contents (e.g., Anders 1964). Based on mineralogy and bulk chemistry, they are divided into the EH (rich in Fe and S) and the EL (low in Fe and S) groups (e.g., Sears et al. 1982) with some unusual ECs that do not fit into either group (e.g., Weisberg and Kimura 2012). Both EH and EL contain a range of petrologic types from unequilibrated EH3 and EL3 to equilibrated EH4-5 and EL4-6 types. Their mineral constituents include Fe-poor silicates, Si-bearing metal, and unusual sulfide and nitride phases that indicate formation under highly reducing conditions (e.g., Keil 1968; Larimer 1968). Under such conditions, the majority of lithophile elements (e.g., Ca,

Mg, K, Na, Mn, and the REEs) can behave as calcophile elements and partition into complex sulfides (e.g., oldhamite, niningerite). The mineralogy and its chemical compositions allow a further distinction: the EH are more reduced than the EL chondrites. The EH chondrites contain niningerite, alkali sulfides and high Si content (2–3 wt%) in the Fe-Ni metal. The EL chondrites have alabandite (e.g., Lin and El Goresy 2002) and less than 1 wt% Si in the Fe-Ni metal (Weisberg et al. 2006).

Enstatite chondrites are the only chondrites with bulk O, Cr, Ti, Ni, and Zn stable isotope compositions similar to those of Earth and the Moon (e.g., Clayton and Mayeda 1984; Warren 2011; Paniello et al. 2012). However, Si isotopes differ from the Earth and Moon (Fitoussi and Bourdon 2012; Savage and Moynier 2013), which may indicate that ECs formed in the inner solar system. The lack of evidence for hydrous alteration of matrix and chondrules also points toward their formation well within the snow line. In addition, the mineralogy and redox state of ECs suggest their formation under similar conditions as the inner planets (e.g., Mercury) (Ebel and Alexander 2011).

ECs have the most reduced and sulfurized mineral assemblages known from meteorites (e.g., Keil 1968; Larimer 1968; Gannoun et al. 2011; Weisberg and Kimura 2012; Lehner et al. 2013; Barrat et al. 2014). To understand the physicochemical conditions prevailing in such regions, several detailed studies have been performed (e.g., Keil 1968, 1984; Sears et al. 1982; Grossman et al. 1985; Rubin and Grossman 1987; Weisberg et al. 1994; Rubin et al. 1997; Kimura and Lin 1999; McCoy et al. 1999) in ECs.

Characterization of the trace element contents of ECs have been carried out by the bulk analysis of fragments of these meteorites (e.g., Hertogen et al. 1983; Sears et al. 1983; Frazier and Boynton 1985; Grossman et al. 1985; Kallemeyn and Wasson 1986; Ebihara 1988); by analysis of the rare earth element (REE) abundances in enstatite grains of unequilibrated ECs (Lundberg and Crozaz 1988; Weisberg et al. 1994; Hsu and Crozaz 1998); by the analysis of REE and other trace elements in enstatite and sulfides (mainly oldhamite and niningerite) (Larimer and Ganapathy 1987; Ebihara 1988; Crozaz and Lundberg 1995; Gannoun et al. 2011); and, recently, by the study of the abundances of a wide variety of trace elements (REEs, Y, Nb, Zr, Hf, Sc, Ba, Rb, Sr, Th, and U) of EH and EL chondrites (Barrat et al. 2014). However, no such studies have been performed for chondrules and chondrule fragments in EH3 and EH4 chondrites.

Here, we report on a petrographic and chemical study of individual nonporphyritic chondrules and chondrule fragments in Sahara 97158 (EH3) and Indarch (EH4) chondrites. We explore whether the trace element relationships of these objects are characteristic for EH3 and EH4 chondrules. Our results give some insights into the chemical features that are distinctive for ECs, the process involved in chondrule formation, and the existence of late metasomatic events acting with variable efficiency during or after chondrule formation. Varela et al. (2014) reported preliminary results.

SAMPLES AND ANALYTICAL METHODS

Sixteen chondrules and/or fragments of chondrules were analyzed in polished thin and thick sections in two enstatite chondrites: 12 objects from the EH3 Sahara 97158 and 4 objects from the EH4 Indarch (Fig. 1). Both samples are from the NHM Vienna (inventory numbers: N3264 and N2137, respectively). Abbreviations of sample names used throughout this paper are: SA = Sahara 97158 and IN = Indarch.

Analytical Techniques

Objects were selected for chemical analysis using an optical microscope and a scanning electron microscope. Major element chemical compositions were obtained with a JEOL 6400 analytical scanning electron microscope (ASEM) (NHM Vienna) and a CAMECA SX100 electron microprobe (Department of Lithospheric Science, University of Vienna). Electron microprobe analyses (EMPA) were performed using a 15 kV acceleration potential and 15 nA sample current. Estimated precision for major and minor elements is better than 3%, for Na about 10%. The detection limits of elements (in ppm) are as follows: Na: 278; Si: 219; Mg: 172; Al: 140; K: 289; Ti: 326; Fe: 573; Mn: 323; Cr: 443; Ni: 491. Natural and synthetic standards were used for calibration and a ZAF correction was applied to the data.

Scans approximately 7.5×10 μm in size were made over several nonoverlapping areas with total dimensions of 80×80 μm and averaged to give estimated bulk compositions. Sulfur was probably not measured representatively, because sulfides usually are not distributed homogeneously inside the objects. Additionally, major element contents of silicate phases were measured by ASEM and EMPA using finer beam sizes. A problem with beam raster analyses is that the ZAF corrections for the bulk composition may be different from those in the individual minerals present. This was not a major problem in previous studies (e.g., Engler et al. 2007) in which only silicates were involved. However, this can lead to errors when phases with greatly different densities, such as metal and sulfide, are present. For the studied samples, the lack of corrections based on density differences (Warren 1997; Berlin et al.

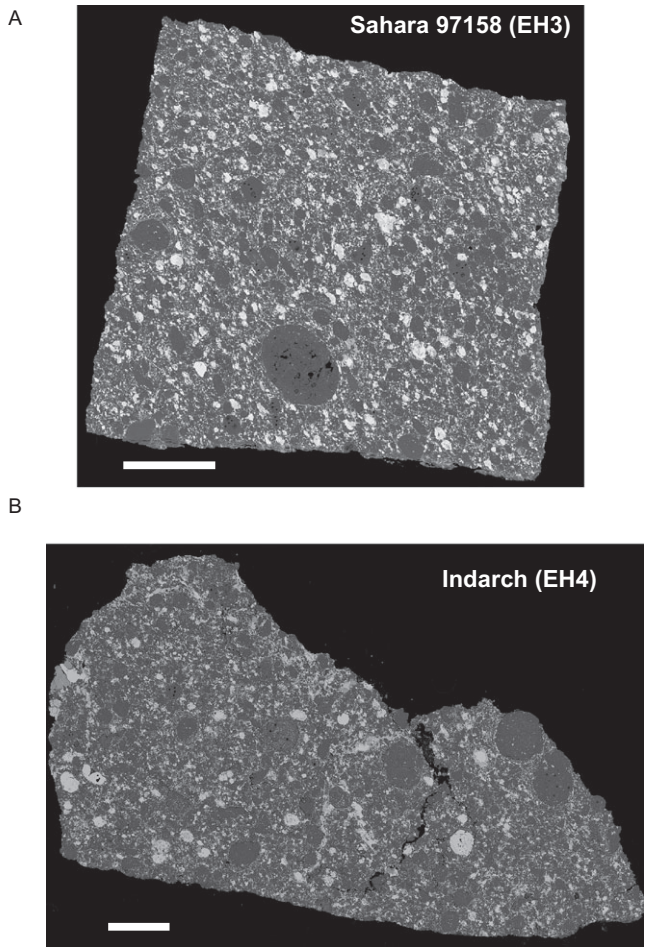

Fig. 1. Backscattered electron images of the studied sections. A) Sahara 97185 (bar scale: 3 mm), B) Indarch (bar scale: 1.6 mm).

2008) will reduce the accuracy of the measured bulk elemental contents.

The bulk trace element contents of the chondrules and chondrule fragments, as well as trace element contents of individual silicate phases within each object, were measured with a VG Plasma Quad II+ "S" ICPMS and a 266 nm Q-switched Nd-YAG laser at the Memorial University of Newfoundland (see Jackson et al. [1992], Jenner et al. [1993], and Jackson [2001] for a detailed description of the system). The laser was pulsed at a frequency of 10 Hz, with an energy of 0.3–0.4 mJ per pulse. The first 40 s of each measurement were acquired with the laser off to determine the background count rates for each analysis. The sample was then ablated for 50–80 s, depending on the stability of the acquired signals and the thickness of the mineral in the section. Ablation pit diameters ranged between 10–40 μm (usually 40 μm), depending on the area of interest and/or the object size. For bulk analyses of the objects, either a 100 × 100 μm box raster or 40 × 100 μm line scan was used, depending on the grain size and homogeneity of chondrules and fragments. Engler et al. (2007) presented the detailed conditions under which trace element analyses were performed, as well as a description of the standardization procedure.

The analytical error is expressed in terms of long-term precision (Table 1), calculated as the relative standard deviation of the average of BCR reference standard analyses, collected over the whole period of measurements (the reference standard was run at least twice in all of the individual sets of analyses).

The various microbeam methods (ASEM, EMPA, and LA-ICP-MS) used for obtaining bulk analyses of micro-objects in thin/thick sections are based on the assumptions that the volume analyzed is representative of the whole object. Thus, the disadvantage of these methods is the possibility of nonrepresentative sectioning of inhomogeneous or coarse-grained objects. Although we tried to measure the true bulk value by making rasters or scans over representative areas (depending on the homogeneity and grain size of each individual object), the bulk analyses by ASEM, EPMA, and LA-ICP-MS should be considered as the best approximation that we could obtain for the actual bulk elemental contents.

RESULTS

Petrography

The studied objects are nonporphyritic chondrules, chondrule fragments, and related objects (Table 2). Their size ranges from about 250 μm–2.5 mm in apparent diameter. Shapes of objects vary between spheroidal (spherical to ellipsoidal) and irregular (Figs. 2A–L). Based on these variations, the objects were divided into the following four groups (using the same nomenclature as in Engler et al. 2007) (a) chondrules (C), (b) chondrule fragments (CF), and (c) irregular objects (IO), the latter being objects that have textures similar to those of chondrules (Table 2).

Grain sizes of mineral phases range from <1 μm to a maximum of about 20 μm. In some cases, single large grains of minerals are present (e.g., SA2, SA8) (Fig. 2D). Most of the objects are dominated by granular textures with minor fibrous and platy textures (Table 2). Although the distinction between porphyritic and granular textures can be subtle, objects with granular textures are typically composed of closely packed anhedral crystals of olivine and/or pyroxene with very low amounts of interstitial mesostasis. The grain size can vary between very fine-grained and coarse-grained. In certain objects, there are transitions between granular

Table 1. Long-term precision of LA-ICP-MS analyses for individual elements (± RSD% of BCR analyses).

Element	± R SD%:	Element	± R SD%:	Element	± R SD %:
Zr	9	La	8	Sr	6
Hf	11	Ce	7	Ba	7
Sc	9	Pr	7	V	4
Y	9	Eu	8	Cr	22
Nb	6	Nd	9	Mn	5
Ta	10	S m	9	Rb	8
Ti	14	Tb	10	Cs	8
Ca	4	Gd	10	W	13
Th	11	Dy	11		
U	9	Ho	11		
		Er	12		
		T m	12		
		Yb	12		
		Lu	12		

textures and platy textures (e.g., SA8, Fig. 2D). Those with platy textures are barred olivine objects (IN4, Fig. 2J) consisting of parallel plates of olivine (which usually are in optical continuity) with interstitial glass.

Radial textures with pyroxene as main mineral phase are scarce among the studied objects (IN6, Fig. 2K). In certain objects pyroxene grew with fibrous shape. A typical system for arranging the fibers is radiating with one or more eccentric locations of the radiation center (e.g., IN6).

The dominant silicate phases of the different objects are low-Ca pyroxene, with minor olivine, high-Ca pyroxene, and glass. Subordinated phases include silica (SA2, SA5, SA7, SA15) and plagioclase (IN6–IN3). Object SA10 is very inhomogeneous with an olivine-rich coarse-grained core (SA10-core) and a thick pyroxene-rich fine-grained rim (SA10-rim) (Figs. 2E and 2F).

Besides troilite, oldhamite is present as a ubiquitous phase in all chondrules, with a minor presence of more exotic, rare sulfides like niningerite and alabandite. Objects in Indarch show metal and sulfides that are often attached to chondrule rims. The principal petrographic characteristics of all studied objects are summarized in Table 2.

Chemical Composition of Individual Phases

Low-Ca pyroxene is the major mineral phase in both chondrites. There is a slight difference in the major element composition of low-Ca pyroxene in Sahara 97158 varying from $En_{89.7\text{-}98.8}$ as compared to in Indarch, which almost reaches pure enstatite endmembers $En_{94.5\text{-}99.5}$.

High-Ca pyroxene is scarce and was only detected in SA3, varying in composition from $Wo_{0.18}$ to $Wo_{25.5}$.

Olivine was identified in three objects (SA2, SA3, SA8) as a minor mineral phase with elemental abundances showing a narrow range from $Fo_{98.6\text{-}96.5}$.

Plagioclase was only detected in objects from EH4 Indarch with almost no variation in the major element composition: $Ab_{96.6}$–$Ab_{98.2}$.

Glass and Si-rich phases: Glass in Sahara 97158 objects contains between 64.3 and 74.4 wt% SiO_2, 10–20 wt% Al_2O_3, 2-18 wt% MgO, 2.7–5.5 wt% Na_2O, and 0.2–7.8 wt% CaO. In objects SA7 and SA12, Si-rich phases (SiO_2: 92.6-96.6 wt%) are present. Glasses in the EH4 Indarch are less Si-rich (~50 wt% SiO_2), but show higher contents in Al_2O_3 and CaO (~30 wt% Al_2O_3 and ~14 wt% CaO) as compared to those present in Sahara 97158.

Representative analyses of mineral phases are listed in Table 3.

Bulk Major and Minor Element Composition

Major element compositions of bulk objects from Sahara 97158 have SiO_2 contents varying from 50 to 64 wt%, Al_2O_3 contents from 0.7 to 4 wt%, apparent FeO contents from 1 to 9.5 wt%, MgO contents from 25 to 34 wt%, and CaO contents from 0.5 to 2.5 wt%. The objects from Indarch have lower SiO_2 (48–59 wt%) and MgO (21–31 wt%) contents, as compared to Sahara 97158. All objects show subchondritic CaO contents with Al_2O_3 contents showing some variation depending on the glass/feldspar ratio of the objects. The $Na_2O + K_2O$ contents vary between 0.1 and 4 wt% (Table 4).

Lithophile Trace Element Abundances

Lithophile trace element abundances in bulk objects of ECs vary mostly between 0.1 and 7 x CI (Figs. 3A and 3B; Table 5). The abundance patterns are generally flat with significant abundance anomalies in Nb, which can be observed in the majority of objects of the two chondrites analyzed.

Objects in Indarch

The EH4 Indarch objects have irregularly fractionated refractory trace element abundances (Fig. 3A). Niobium is strongly depleted in IN4 and IN7 relative to the other refractory elements. CI chondrite-normalized REE patterns are relatively flat with IN4 showing a slight negative Ce anomaly. A strong depletion in Yb is present in object IN6 relative to the other HREE. The abundances of the more refractory of the moderately volatile elements (Sr and Ba) are variable, with objects showing positive (IN4, IN7) and

Table 2. (a) Petrography of Sahara 97158 (EH3) objects and (b) petrography of Indarch (EH4) objects.

Object	Shape	Diameter	Texture	Max. grain size	Surface features	Mineralogy	Annotations
(a)							
SA1	CF partly rounded	800 μm	GP (granular)	20 μm		Two different low-Ca px, M/S	Px is inhomogeneous (Fe) sulfides: troilite, niningerite alabandin
SA2	C ellipsoidal	610 μm	GP (granular)	40 μm	Irregular surface	Low-Ca px, ol, sulfides, glass, SiO_2	One coarse-grained ol crystal; in outermost part prevailing glass; sulfides: troilite, heideite, oldhamite
SA3	C ellipsoidal	800 μm	GPO (granular)	<10 μm	Local coarse M/S grains attached	Low-Ca px, ol, high-Ca px, M/S	Px rims Ca-enriched; sulfides: troilite, oldhamite
SA5	IO irregular	800 μm	GP (granular)	30 μm	Irregular surface local M/S grains attached	Low-Ca px, glass, SiO_2, M/S	Local alteration (+Fe); sulfides: troilite, oldhamite
SA6	C spherical	130 μm	GP (granular)	<7 μm	Local M/S grains attached	Low-Ca px, glass, M/S	Local alteration (+Fe); M/S; and glass grains are very fine
SA7	IO irregular	700 μm	GP (granular)	7 μm	Irregular surface local M/S grains attached	Low-Ca px, glass, SiO_2, M/S	Inhomogeneous px composition; M/S grains are very fine (no quantitative analyses possible)
SA8	C ellipsoidal	470 μm	GP(granular platy)	20 μm	Irregular surface local M/S grains attached	Low-Ca px glass, sulfides	One coarse-grained px-crystal in the (200 μm); sulfides: troilite, oldhamite in outermost part prevailing glass; inhomogeneous px composition
SA9	CF partly rounded	400 μm	GP (granular)	<10 μm	Irregular surface local M/S grains attached	Low-Ca px, glass, M/S	Along cracks + Fe (alteration) M/S grains are very fine
SA10	C ellipsoidal	2.6 μm	very inhomo-geneous	Inhomogeneous	Irregular surface local M/S grains attached	Ol, mes, low-Ca px glass, sulfides	Center: ol with mesostasis; surrounded by px; and glass; sulfides: troilite, oldhamite and more exotic phases; large voids
SA12	IO irregular	400 μm	GP (granulr)	<40 μm	Irregular surface local M/S grains attached	Low-Ca px, glass, M/S	

Table 2. *Continued.* (a) Petrography of Sahara 97158 (EH3) objects and (b) petrography of Indarch (EH4) objects.

Object	Shape	Diameter	Texture	Max. grain size	Surface features	Mineralogy	Annotations
SA13	C ellipsoidal	630 μm	GP (fine platy - granular)	<20 μm	Irregular surface local M/S grains attached; round depression (100 pm)	Low-Ca px, glass, sulfides	Px forms grains, and plates; local alteration (+Fe)
SA15	C ellipsoidal	300 μm	GP (granular)	10 μm	Irregular surface local M/S grains attached	Low-Ca px, glass, SiO_2, M/S	Local alteration (+Fe)
(b)							
IN3	C spherical	700 μm	GP (granular)	<20 μm		Low-Ca px, plag/glass? sulfides	Many sulfide grains inside the object (troilite, oldhamite)
IN4	CF rounded	320 μm	BO (platy)	10 μm	Irregular surface	Low-Ca px, glass, plag, sulfides	Many sulfide grains in the object (troilite, oldhamite, niningerite); px forms grains or plates
IN6	CF partly rounded	290 μm	RP (platy)	10 μm	Irregular surface	Low-Ca px, plag/glass? sulfides	Sulfides: troilite, oldhamite, niningerite
IN7	CF ellipsoidal	250 μm	GP (granular)	<5 μm	Irregular surface	Low-Ca px, glass, plag, sulfides	Inhomogenous structure due to secondary Ca-enrichment (px); sulfides: troilite, niningerite

C = Chondrule; IO = irregular object; CF = chondrule fragment. For the textures of objects the terminology scheme of Gooding and Keil (1981) was used: G for granular objects, R for radiating objects, followed by P for pyroxene (as major phase); M/S means metal and sulfides

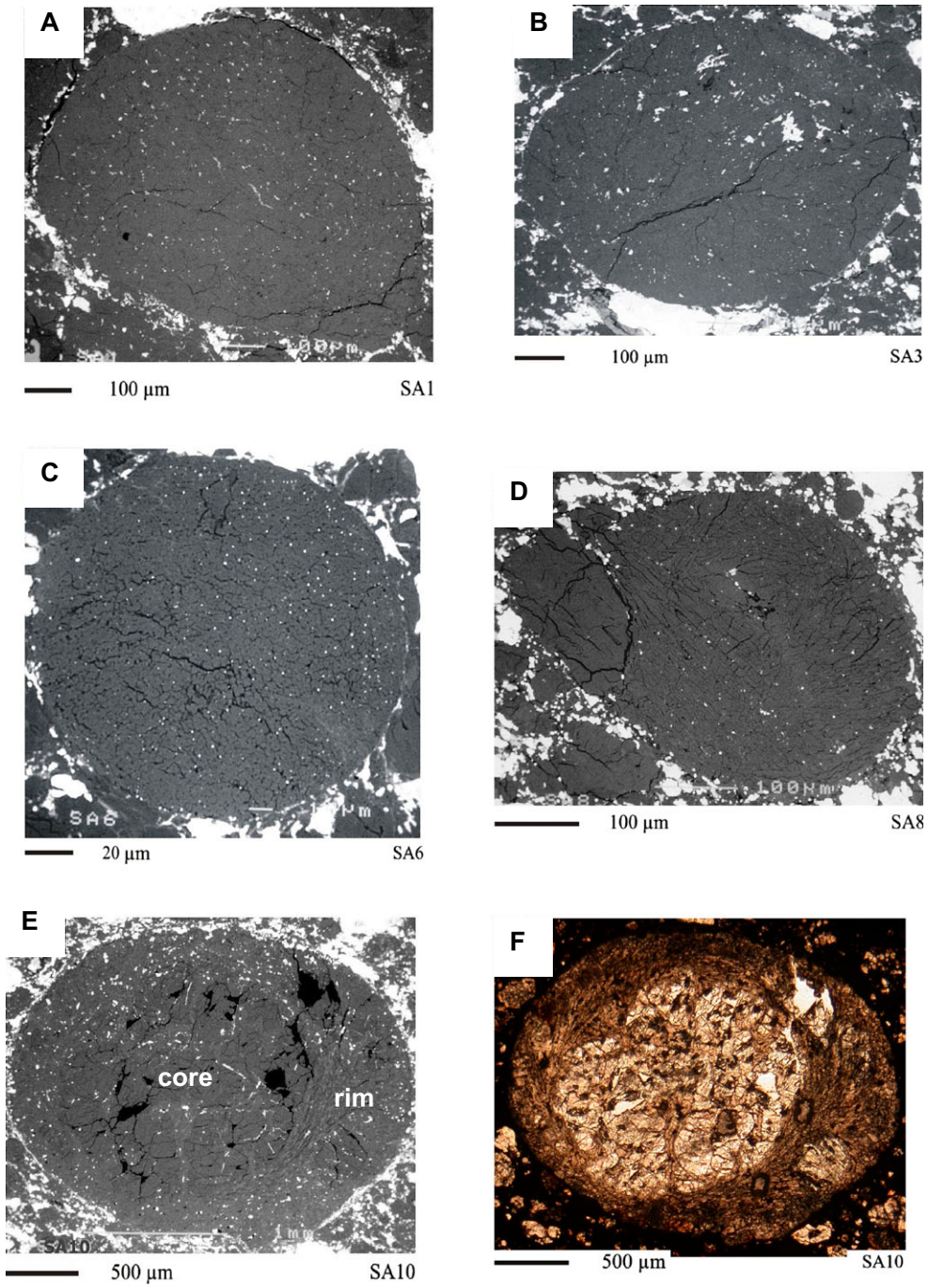

Fig. 2. A–H) Backscattered electron images of objects from Sahara 97158. F) Transmitted light optical image of layered object SA10 in which the core and rim are observed. I–L) Backscattered electron images of objects from Indarch.

negative (IN3, IN6) anomalies. The studied objects display a strong negative V anomaly (except IN3) with all four chondrules having a positive Cs anomaly.

Objects in Sahara 97158

The unequilibrated EH3 Sahara 97158 shows roughly flat, CI chondrite-normalized trace element abundance patterns ranging mostly between 1 and 5 x CI, with some irregularities (Fig. 3B; Table 5). The REE patterns are nearly flat in all objects, except for a negative Eu anomaly. The moderately volatile elements are irregularly fractionated, with Sr and Ba being depleted or enriched with respect to the other moderately volatile elements. Objects in Sahara 97158 were divided in two

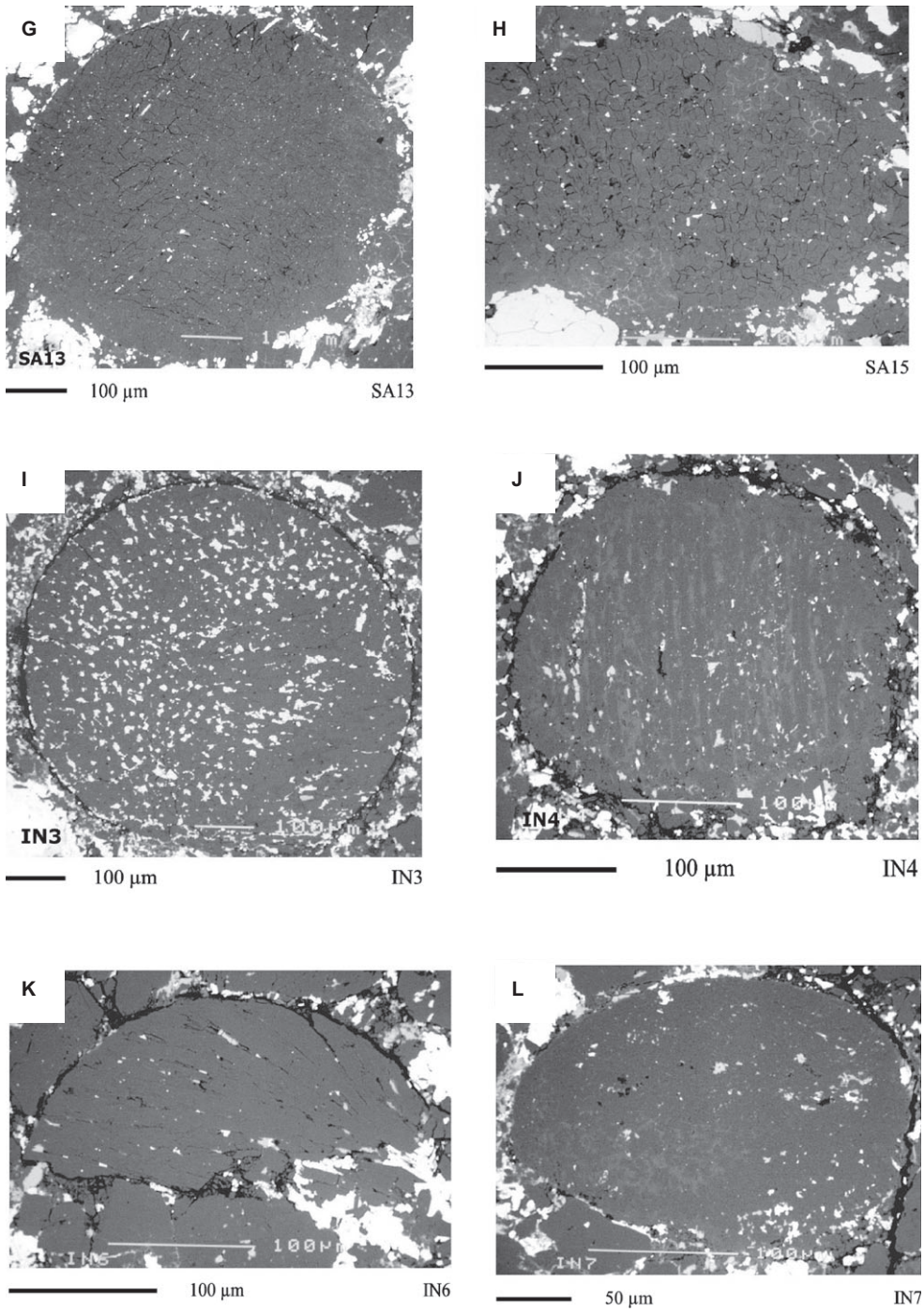

Fig. 2. (Continued).

groups (Figs. 4A and 4B) according to the presence or absence of negative Nb anomalies, as follows.

Objects SA2, SA5, SA7, SA9, SA12, and SA13 have similar abundance patterns of refractory elements with negative abundance anomalies for Nb (strongly depleted in objects SA2 and SA5) (Fig. 4A; Table 5). CI chondrite-normalized REE patterns are flat with Eu below the detection limit in objects SA7, SA9, SA12, and SA13, and showing a slight negative depletion in SA2 and SA5. Additionally, a small positive Tm anomaly is present in SA9 and SA7. The abundances of Sr and Ba are highly variable showing positive and negative anomalies, with object SA7 showing a strong depletion in both elements. The moderately volatile

Table 3. Representative EMP analyses of pyroxene, olivine, plagioclase, glass, and Si-rich phases in Sahara 97158 and Indarch.

Object	SA1	SA2	SA3	SA3.1	SA3.2	SA5	SA6	SA7	SA8	SA8.1	SA8.2	SA9	SA10	SA12	SA13	SA15
Sahara 97158 pyroxene																
SiO_2	55.6	60.5	52.1	54.8	59.5	59.6	60.0	59.7	59.7	60.7	59.5	59.4	59.9	59.5	59.7	59.7
TiO_2	0.14	0.06	0.45	0.25	0.02	0.11	0.10	0.03	0.04	0.07	0.06	0.06	0.07	0.02	0.02	0.02
Al_2O_3	3.1	0.30	6.8	5.4	0.58	0.42	0.49	0.22	0.19	0.26	0.24	0.26	0.35	0.17	0.26	0.17
Cr_2O_3	0.61	0.61	1.06	0.83	0.08	0.30	0.96	0.49	0.47	0.47	0.30	0.25	0.48	0.56	0.44	0.51
FeO	4.1	1.24	2.3	2.8	0.40	0.44	3.2	0.79	1.25	1.33	1.14	0.61	0.75	2.15	0.98	1.09
MnO	0.12	0.19	0.12	0.11	0.02	0.24	0.07	0.24	0.13	0.14	0.07	0.30	0.19	0.16	0.19	0.26
MgO	33.8	36.4	24.8	33.9	39.5	37.5	34.0	37.4	37.3	36.5	39.4	39.0	39.5	37.7	38.2	38.3
CaO	2.06	0.31	12.4	2.6	0.33	0.60	0.83	0.29	0.23	0.22	0.10	0.54	0.30	0.19	0.19	0.26
Na_2O	0.02	0.05	0.11	b.d.	0.08	0.05	0.05	0.08	0.03	0.05	b.d.	0.11	b.d.	b.d.	0.03	b.d.
K_2O	b.d.	0.03	b.d.	b.d.	0.04	0.00	b.d.	b.d.	b.d.	b.d.	b.d.	b.d.	b.d.	b.d.	0.02	b.d.
Total	99.6	99.7	100.1	100.8	100.6	99.2	99.6	99.3	99.4	99.8	100.8	100.5	101.6	100.4	100.1	100.3
Wo	3.9	0.6	25.5	4.9	0.6	1.1	1.6	0.6	0.4	0.4	0.2	1.0	0.5	0.3	0.0	0.5
En	89.7	97.3	70.7	90.6	98.8	97.9	93.4	97.9	97.5	97.4	98.1	97.7	98.2	96.3	98.0	97.6
Fs	6.3	2.1	3.8	4.4	0.6	1.0	5.0	1.5	2.0	2.2	1.7	1.3	1.3	3.3	1.7	1.9

Object	IN3	IN4	IN6	IN7
Indarch pyroxene				
SiO_2	59.4	60.5	59.8	60.4
TiO_2	0.03	b.d.	0.02	b.d.
Al_2O_3	0.24	0.36	0.15	0.15
Cr_2O_3	0.84	b.d.	0.31	0.01
FeO	3.2	0.24	0.88	0.28
MnO	0.18	0.03	0.20	0.02
MgO	36.0	38.6	38.3	39.1
CaO	0.24	0.25	0.23	0.08
Na_2O	b.d.	0.14	0.05	0.03
K_2O	b.d.	b.d.	b.d.	b.d.
Total	100.1	100.1	99.9	100.1
Wo	0.5	0.5	0.4	0.1
En	94.5	99.1	98.0	99.4
Fs	5.0	0.4	1.6	0.4

Table.3 *Continued*. Representative EMP analyses of pyroxene, olivine, plagioclase, glass, and Si-rich phases in Sahara 97158 and Indarch.

Object	SA2	SA3	SA10
Sahara 97158 olivine			
SiO_2	42.6	42.2	42.9
TiO_2	b.d.	0.10	b.d.
Al_2O_3	b.d.	b.d.	b.d.
Cr_2O_3	0.39	0.09	0.39
FeO	1.25	3.4	1.34
MnO	0.17	0.06	0.15
MgO	54.8	53.3	54.5
Total	99.3	99.0	99.3
Fo	98.6	96.5	98.5
Fa	1.3	3.5	1.4

Object	IN3	IN4	IN4.1	IN6	IN6.1	IN7	IN7.1
Indarch–plagioclase							
SiO_2	68.1	68.4	69.5	69.5	70.9	67.9	68.8
TiO_2	0.2	0.3	0.1	0.1	0.2	0.4	0.3
Al_2O_3	19.4	20.2	18.9	19.0	17.8	19.0	18.8
FeO	1.4	0.4	0.4	0.5	0.3	0.8	0.4
MnO	0.4	0.2	0.1	0.1	0.1	0.3	0.1
MgO	0.4	0.4	b.d.	0.7	1.5	0.8	0.5
CaO	0.1	0.8	0.3	0.1	0.2	0.3	0.2
Na_2O	8.6	8.2	9.7	8.6	8.0	8.5	9.4
K_2O	0.2	0.2	0.3	0.2	0.2	0.3	0.3
Total	98.7	99.1	99.1	98.9	99.3	98.2	98.9
Ab	98.2	93.5	96.4	97.8	96.8	96.2	96.6
An	0.4	4.9	1.7	0.7	1.5	1.8	1.1
Or	1.4	1.6	1.9	1.5	1.7	2.0	2.3

Table.3 *Continued*. Representative EMP analyses of pyroxene, olivine, plagioclase, glass, and Si-rich phases in Sahara 97158 and Indarch.

Object	SA2	SA5	SA5.1	SA5.2	SA7	SA7.1	SA10	SA10.1	SA12	SA15
Sahara 97158 glass and Si-rich phases										
SiO_2	64.3	66.1	65.2	73.2	65.2	92.6	68.7	74.4	96.6	67.9
TiO_2	0.4	0.24	0.20	0.02	0.0	b.d.	0.30	b.d.	0.02	b.d.
Al_2O_3	19.8	19.3	21.3	18.4	10.7	1.3	18.0	15.2	0.19	20.3
Cr_2O_3	0.2	n.a.	n.a.	b.d.	0.2	b.d.	n.a.	b.d.	0.03	0.0
FeO	0.3	0.13	0.24	0.20	0.2	0.2	0.14	0.32	0.17	0.2
MnO	0.1	0.05	b.d.	0.00	0.1	0.0	0.04	b.d.	0.01	b.d.
MgO	2.7	2.18	0.42	1.35	18.1	2.9	2.00	0.09	2.04	0.8
CaO	7.6	6.7	7.8	0.22	0.2	0.1	7.5	5.0	0.04	7.5
Na_2O	4.4	4.5	4.7	5.5	5.0	0.7	3.6	2.7	0.10	4.2
K_2O	0.3	0.13	0.14	1.03	0.3	b.d.	0.15	0.32	0.02	0.1
Total	100.1	99.34	99.93	99.9	100.0	97.9	100.35	98.1	99.2	101.0

Object	IN4	IN7
Indarch glass		
SiO_2	47.4	51.8
TiO_2	0.03	0.2
Al_2O_3	33.0	28.8
Cr_2O_3	b.d.	0.2
FeO	0.21	0.6
MnO	b.d.	0.1
MgO	0.85	1.0
CaO	16.1	12.6
Na_2O	2.71	3.4
K_2O	0.04	0.3
Total	100.4	98.9

b.d. = below dedection limit; Na, Ca, K = below dedection limit.

Table 4. Bulk analyses of objects in enstatite chondrites; major and minor elements were measured by SEM and EMPA.

Chondrite	Object	SiO_2	TiO_2	Al_2O_3	Cr_2O_3	FeO	MnO	MgO	CaO	Na_2O	K_2O	P_2O_5	S	Total
Indarch	IN4	50.4	0.1	10.2	0.1	6.7	0.1	20.6	2.8	3.6	b.d.	0.2	2.0	96.8
	IN7	54.7	0.2	8.6	0.3	5.0	0.5	21.0	0.8	4.0	0.1	0.2	1.7	97.1
	IN3	48.4	0.1	1.3	0.8	11.9	0.3	26.1	0.5	1.8	b.d.	0.1	3.4	94.7
	IN6	59.7	0.3	2.5	0.4	2.1	0.1	31.3	0.9	0.2	0.1	0.2	0.8	98.6
Sahara 97158	SA1	49.7	0.7	3.8	0.9	9.5	0.4	29.3	2.4	0.4	0.3	0.3	0.9	98.6
	SA2	62.4	0.4	2.8	0.6	2.1	0.2	28.0	1.7	0.5	0.1	0.1	0.5	99.4
	SA3	53.0	0.5	4.0	0.8	5.1	0.3	30.0	2.5	0.2	0.3	0.3	1.1	98.1
	SA5	57.9	0.3	4.1	0.6	2.7	0.2	29.2	2.0	0.8	0.3	0.2	0.7	99.0
	SA6	58.9	0.2	0.7	1.1	3.4	0.2	33.9	0.8	0.1	0.1	b.d.	0.1	99.4
	SA7	60.2	0.2	1.9	0.6	6.3	0.3	26.8	0.2	b.d.	0.1	0.1	1.1	97.8
	SA8	62.8	0.1	0.8	0.5	1.1	0.1	33.1	0.4	0.5	0.1	0.1	0.2	99.8
	SA9	60.5	0.4	2.1	0.4	5.1	0.3	27.7	0.6	0.8	0.2	0.2	0.7	99.0
	SA10 (c + r)	48.5	0.2	1.5	0.5	4.7	0.4	39.8	1.0	0.4	0.1	0.1	1.0	98.1
	SA12	64.5	0.1	2.6	0.6	3.4	0.2	25.9	0.5	0.4	0.2	0.2	0.6	99.2
	SA13	59.6	0.5	2.8	0.4	6.5	0.2	25.9	0.9	0.8	0.2	0.1	0.7	98.6
	SA15	63.4	0.3	3.4	0.7	3.4	0.2	25.0	1.4	0.3	0.3	0.2	0.5	99.1

b.d. = below dedection limit; c + r = core and rim.

elements Mn, V, Cr, Rb, and Cs have normalized abundances that increase smoothly with increasing volatility.

Objects SA3, SA1, SA8, and SA15 have similarly flat normalized abundance patterns for refractory and REE elements (Fig. 4B). They do not have a deficit in the Nb abundances but show Eu negative anomalies. Their abundances in Sr and Ba are variable as are also those of the volatiles Rb and Cs.

The object SA10 (visible in the lower central part of the polished section, Fig 1A) is the biggest chondrule in Sahara 97158. The two analyses of SA10 (SA10-core stands for the coarse-grained inner portion and SA10-rim stands for the fine-grained outer portion) have nearly flat CI chondrite-normalized refractory trace element patterns with abundances around 2–4 × CI (Fig. 4C). Both analyses show negative Nb anomalies, which are strongly depleted in the core of the object. The REE patterns are rather flat with a negative Eu anomaly. Abundances of Sr and Ba are variable relative to the REE. The moderately volatile elements Mn, V, Cr, Rb have normalized abundances that increase smoothly with increasing volatility, with a slight depletion in Cs.

Elements with different geochemical and cosmochemical properties (Yb and Ce) are plotted against each other in Fig. 5A. The trace element ratios of objects in Sahara 97158 and Indarch show a positive correlation of elemental abundances with almost all objects lying on or very close to the solar line.

DISCUSSION

Porphyritic chondrules are the dominant textural type of chondrule in the unequilibrated ECs. They consist of near endmember enstatite (with scarce olivine), glass of albitic composition, silica and minor Fe-Ni metal, and sulfides (mainly troilite containing variable amounts of Mn-Mg-CaS) (e.g., Weisberg and Kimura 2012).

The presence of relic, FeO-bearing olivine (Rambaldi et al. 1983; Lusby et al. 1987; Weisberg et al. 1994) among the highly reduced mineralogy of chondrules in ECs indicates prechondrule processing in an oxidizing environment (Kurat 1988). Accordingly, chondrules in ECs may have originated from source materials depleted in sulfides. Subsequent sulfurization (by S^{2-} metasomatism) formed sulfides from metal and silicates. Evidence for this is replacement of enstatite and forsterite by the assemblage of a silica phase and sulfides containing Mg, Mn, Fe, Ca, and Na (Lehner et al. 2010, 2013). The variable mineralogical and bulk chemical compositions of different clasts of ECs reflect variable degrees of sulfurization in the chondrule-forming environment. An example of more sulfurized objects are the silica-bearing chondrules with abundant niningerite ([Mg,Fe,Mn]S) and troilite in the unequilibrated EH chondrites.

Sulfurization may have occurred during either chondrule accretion and/or later metamorphism at low CO fugacities (Fleet and MacRae 1987). Thermodynamic data for the observed mineral reactions show that formation of SiO_2 and sulfides via sulfidation reactions can be achieved by lowering f_{O2}, increasing f_{S2}, or a combination of the two (Petaev et al. 2011). In the solar nebula, the chondrule-forming regions could have been located closer to the proto-Sun where the gas pressure was high (e.g., 0.1–1.0 bar) (Blander et al. 2009). Accordingly, under such conditions, formation of

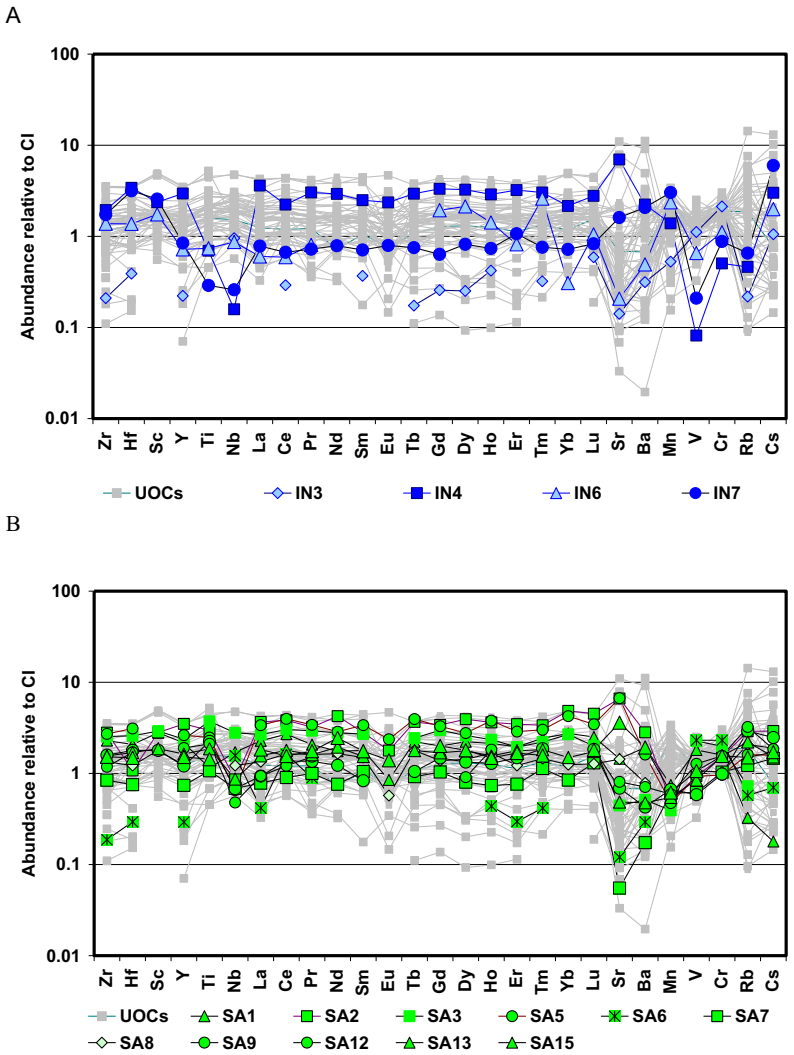

Fig. 3. Bulk analyses of lithophile trace elements normalized to Cl chondrite abundances (here and in the following graphs, normalizing data were taken from Lodders and Fegley 1998) of all studied objects in: A) Indarch and B) Sahara 97158, compared to those of UOCs (Engler et al. 2007).

chondrules in ECs could take place by direct condensation (applying the Constrained Equilibrium Theory). Blander et al. (2009) suggested that chondrules were formed by solidification of supercooled liquid rain-like droplets in equilibrium with the nebula gas rather than by remelting of preexisting matter produced liquid droplets. Their calculations suggest that nucleation and crystallization of silicate droplets took place at ~1400 K. This model seems to rest on the idea that surface tension governs the nucleation of liquid, suppressing Fe condensation. Therefore, the presence of small relict, prechondrule, and/or presolar grains that could have acted as seeds for nucleation appear to restrict this model.

Engler et al. (2007) argued that nonporphyritic objects from UOCs were the result of direct condensation in a late stage of evolution of the solar nebula, based on petrographic and chemical data and theoretical considerations. Major and trace element compositions of the objects have unfractionated (solar-like) ratios of CaO/Al_2O_3, Yb/Ce, and Sc/Yb. Their full equilibrium condensation calculations show that it is possible to have enstatite as the stable liquidus phase in an 800 × Cl dust-enriched nebular gas at a p_{tot} of 10^{-3} atm, if about 72% of the original Mg is removed (possibly as forsterite) from the system. Besides Mg depletion by olivine removal, several cosmochemical processes could have removed Mg from the system efficiently, such as by separating Mg under reducing conditions (forming sulfides). Such a process was very likely active in the enstatite chondrite formation regions because these meteorites contain pyroxene-rich and

Table 5. Trace element analyses of objects in Sahara 97158 and Indarch enstatite chondrites (LA-ICP-MS analyses in ppm, except Ti in wt%).

Chondrite	Indarch				Sahara 97158											
object	IN3	IN4	IN6	IN7	SA1	SA2	SA3	SA5	SA6	SA7	SA8	SA9	SA10 rim	SA10 core	SA12	SA13
Zr	0.82	7.57	5.37	6.75	8.94	10.92	9.90	10.58	0.73	3.28	5.22	6.19	9.34	6.94	4.61	6.07
Hf	0.04	0.36	0.14	0.33	0.22	0.11	0.27	0.33	0.03	0.08	0.13	0.19	0.25	0.18	0.18	0.18
Sc	b.d.	13.97	10.29	15.13	16.49	16.57	17.19	b.d.	b.d.	b.d.	10.57	10.55	10.30	11.25	b.d.	11.02
Y	0.35	4.61	1.12	1.32	3.37	5.45	3.70	4.10	0.46	1.15	1.92	1.88	3.92	2.97	2.96	2.55
Ti	0.03	0.03	0.03	0.01	0.07	0.13	0.16	0.11	0.05	0.05	0.09	0.10	0.12	0.07	0.09	0.08
Nb	0.24	0.04	0.22	0.06	0.43	0.21	0.70	0.16	0.39	0.17	0.31	0.17	0.46	0.10	0.12	0.22
Th	0.00	0.07	b.d.	0.02	0.05	0.11	0.09	0.09	0.01	0.03	0.05	0.06	0.09	0.06	0.04	0.04
U	b.d.	0.10	b.d.	b.d.	0.03	0.07	0.04	b.d.	0.02	0.08	0.01	0.03	0.05	0.02	0.03	0.03
La	b.d.	0.85	0.14	0.18	0.54	0.86	0.63	0.79	0.10	0.18	0.32	0.22	0.70	0.46	0.22	0.37
Ce	0.18	1.38	0.37	0.41	1.67	2.38	1.88	2.46	1.00	0.56	1.02	0.85	1.99	1.38	0.75	1.11
Pr	b.d.	0.29	0.08	0.07	0.19	0.30	0.28	0.32	0.08	0.09	0.15	0.13	0.27	0.19	0.14	0.15
Nd	b.d.	1.35	b.d.	0.36	0.81	1.96	1.28	1.32	b.d.	0.35	0.76	0.56	1.36	1.08	b.d.	0.89
Sm	0.06	0.37	b.d.	0.11	0.27	0.42	0.41	0.51	b.d.	0.16	0.22	0.12	0.40	0.33	b.d.	0.23
Eu	b.d.	0.13	b.d.	0.05	0.05	0.10	b.d.	0.14	b.d.	b.d.	0.03	b.d.	0.12	0.07	b.d.	b.d.
Tb	0.01	0.11	b.d.	0.03	0.08	0.14	0.09	0.15	b.d.	0.03	0.07	0.04	0.10	0.07	b.d.	0.07
Gd	0.05	0.66	0.39	0.13	0.40	0.68	0.60	0.66	b.d.	0.21	0.28	0.30	0.57	0.41	b.d.	0.34
Dy	0.06	0.81	0.53	0.20	0.56	0.98	0.65	0.69	b.d.	0.20	0.36	0.33	0.75	0.56	0.23	0.44
Ho	0.02	0.16	0.08	0.04	0.12	0.20	0.13	0.21	0.02	0.04	0.09	0.07	0.16	0.12	0.10	0.09
Er	b.d.	0.52	0.13	0.17	0.31	0.56	0.31	0.46	0.05	0.12	0.20	0.24	0.49	0.37	b.d.	0.28
Tm	0.01	0.08	0.06	0.02	0.06	0.08	0.06	0.08	0.01	0.03	0.04	0.05	0.06	0.05	b.d.	0.05
Yb	b.d.	0.34	0.05	0.12	0.44	0.78	0.43	0.68	b.d.	0.14	0.20	b.d.	0.36	0.27	b.d.	0.24
Lu	0.01	0.07	0.03	0.02	0.06	0.11	0.05	0.09	b.d.	0.03	0.03	0.05	0.08	0.06	b.d.	0.04
Sr	1.0	50.9	1.5	11.8	10.6	48.4	3.2	48.9	0.88	0.40	10.4	5.0	34.8	9.5	5.9	3.5
Ba	0.74	5.3	1.2	4.9	4.5	6.6	1.2	3.8	0.69	0.41	1.8	1.0	5.0	1.4	1.7	1.1
Mn	0.10	0.27	0.46	0.59	0.14	0.10	0.08	0.09	0.04	0.12	0.07	0.13	0.07	0.07	0.11	0.11
V	61.4	4.49	36.1	11.5	99.4	51.4	124	50.9	127	33.9	58.6	32.1	32.8	41.7	70.0	46.5
Cr	5644	1338	2940	2329	4210	4013	5274	2555	6124	2741	2749	2605	2388	2144	4128	4117
Rb	0.50	1.06	b.d.	1.51	0.75	6.66	1.66	3.70	1.32	2.81	4.77	6.70	4.57	4.90	7.43	5.09
Cs	0.20	0.57	0.38	1.14	0.03	0.55	b.d.	0.30	0.13	0.28	0.36	0.47	0.30	0.25	0.35	0.29

b.d. = below dedection limit.

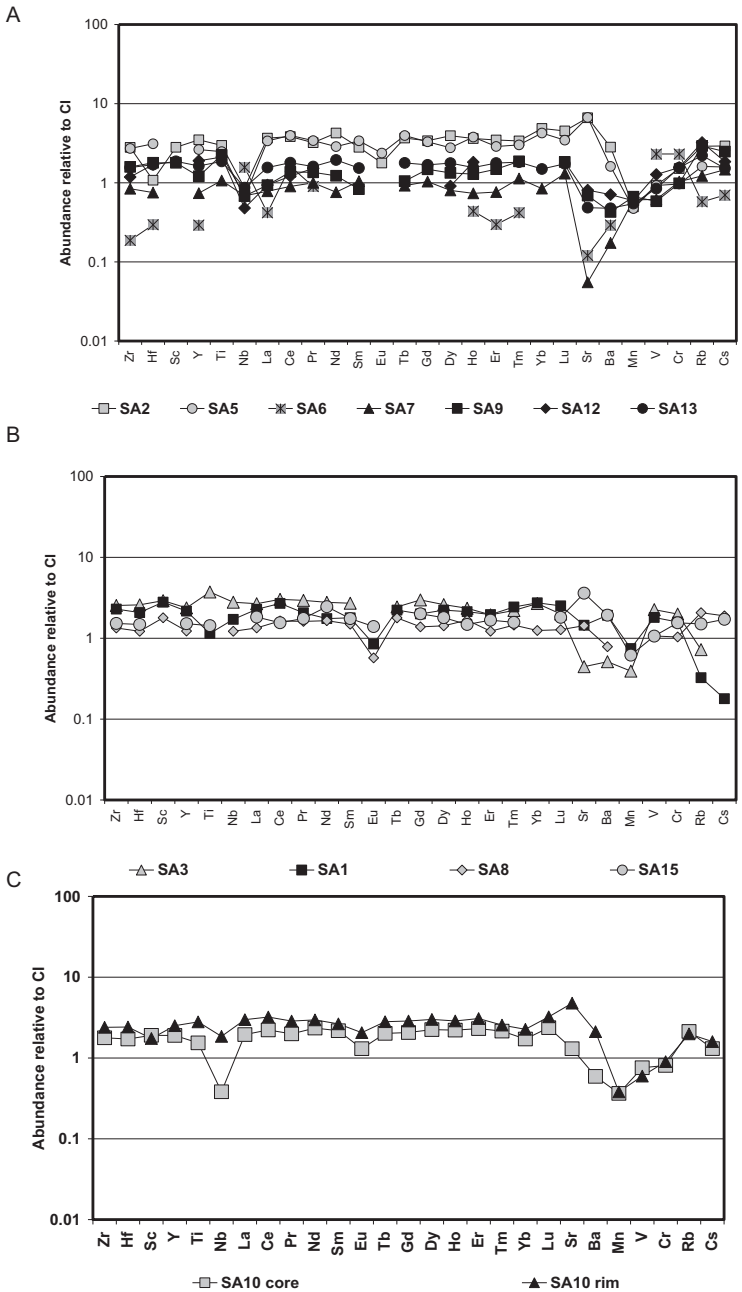

Fig. 4. Bulk analyses of lithophile trace elements normalized to Cl chondrite abundances of objects from Sahara 97158. Objects are divided into two groups according to the presence (A) or absence (B) of a negative Nb anomaly. Several objects have Eu contents below the detection limit. C) Object SA10: core and rim.

SiO_2-oversaturated chondrules, an indication of a highly fractionated Mg/Si ratio.

In this study, the trace element data in nonporphyritic chondrules in ECs show that these objects could have been formed via cosmochemical (rather than geochemical) processes. In contrast to UOCs (Engler et al. 2007), some of the refractory elements in the ECs appear to have been fractionated from the primordial ratio, possibly during sulfide formation. However, addition of alkali elements from the vapor to the cooling chondrule was apparently a common process in nonporphyritic chondrules of both UOCs and ECs. Grossman et al. (2002) suggested that zoning of moderately volatile elements in Semarkona chondrules was due to hydration of chondrule glass without devitrification during aqueous alteration. However, detail studies of nondevitrified alkali-rich glasses in glass inclusions and mesostasis in

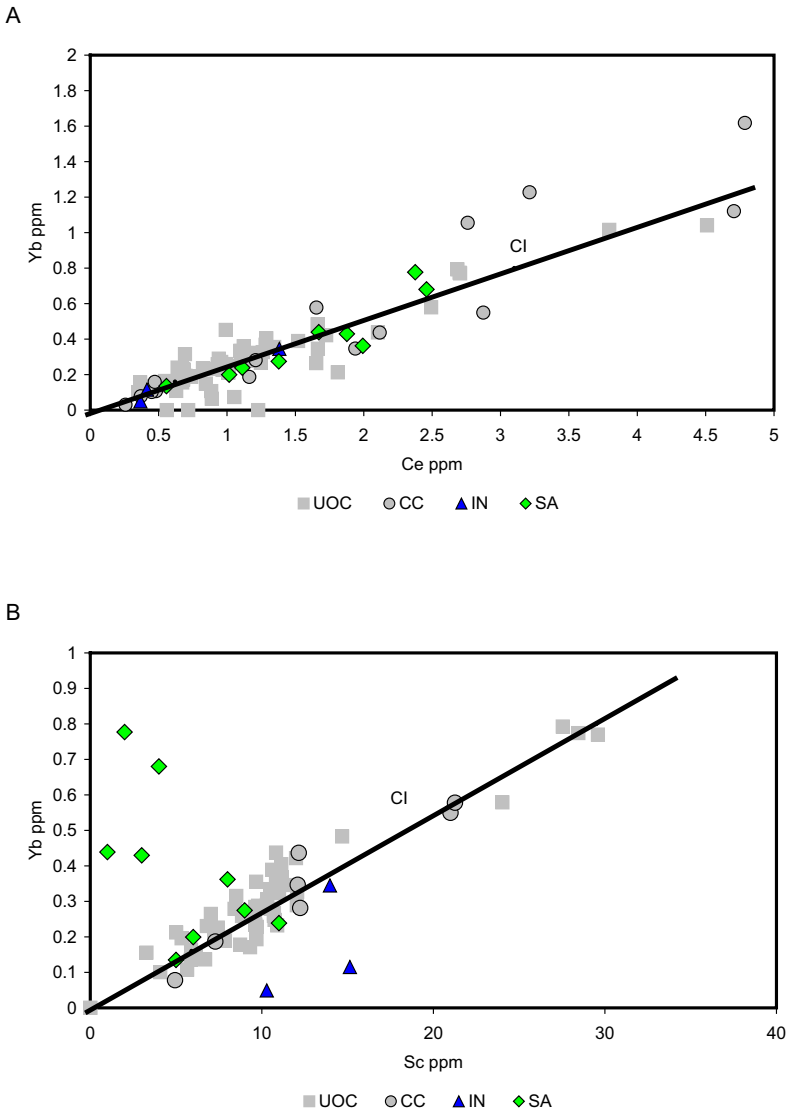

Fig. 5. Element correlation plots for (A) Yb versus Ce, B) Yb versus Sc. Data of nonporphyritic objects in unequilibrated ordinary chondrites (UOCs) (Engler et al. 2007) and carbonaceous chondrites (Engler et al. 2003) are given for comparison.

chondrules of carbonaceous and ordinary chondrites show that the hydration process will produce devitrification. The presence of nondevitrified glasses could signal some other process, like a Ca versus alkalis exchange reaction (e.g., Varela and Kurat 2009). In the studied objects, alkali addition was accomplished with variable efficiency, with only a few objects managing to fully equilibrate their moderately volatile and volatile element abundances with the chondritic reservoir.

Major Elements

Nonporphyritic chondrules and chondrule fragments of Sahara 97158 and Indarch have MgO and SiO_2 rich compositions. The variable Fe contents (with Fe^{tot} calculated as apparent FeO) largely reflect the variable amounts of metal and sulfide carried by the objects. It was not possible to measure bulk silicate compositions of the chondrule objects using microbeam methods without also including some metallic Fe (Table 4). Bulk silicate analyses of objects in ECs, including silicate glass (see Table 3), do not commonly contain FeO, reflecting the reducing environment in which they formed. The high Al_2O_3 contents of some objects from Indarch (IN4, IN7) are mainly a consequence of their high abundance of Al-rich glass and feldspar.

The sums of the volatile components $K_2O + Na_2O$ plotted against the refractory oxide Al_2O_3 scatter

roughly around the CI line (Fig. 6A). This is suggestive of variable addition of alkalis from the vapor to the cooling chondrule. Because Na and K have slightly different condensation temperatures (e.g., Lodders 2003) the final Na/K ratio of the studied objects will depend on how long each object resided in particular regions of the nebular gas. The weak correlation shown in Fig. 6A may indicate that the equilibration process with the chondritic reservoir did not run to completion.

The oxides Al_2O_3 and CaO are both refractory and should not be cosmochemically fractionated from each other if the objects were generated as condensates (as discussed below). A fractionation could mean that either the objects evolved in an environment with a composition different from the solar composition or later subsolidus reactions separated the elements. In the studied objects, a weak correlation between CaO and Al_2O_3 exists, with CaO/Al_2O_3 lower than chondritic values (Fig. 6B). This Ca-deficit could be the result of a fractionation mechanism that is peculiar to enstatite chondrites. Crystallization of sulfides such as oldhamite would fractionate the CaO/Al_2O_3 ratio because Ca (due to its calcophile behavior) is in part partitioned into sulfides.

The Refractory and REE Elements

Figure 5A plots the compatible/refractory element Yb against the incompatible/refractory element Ce and the compatible/refractory element Sc. The abundances of Yb and Ce are well correlated with almost all objects lying close to or on the primordial ratio. Yb and Ce have different geochemical behavior but these elements are not fractionated, indicating that the objects did not change their solar ratios for these elements during their evolution. This, points to the predominance of a cosmochemical process (condensation) during formation of these chondrules. Objects with pyroxene-dominated mineralogy of the ECs show mostly unfractionated RLTE patterns with or without specific abundance anomalies, as discussed below. Mixing and melting of solid precursors cannot produce these patterns. If this is the case, we should expect some fractionation of REE abundance patterns, as well as fractionated Yb/Ce ratios according to the mineralogy of the objects. The fact that we do not see these fractionations, despite the SiO_2/MgO fractionation, suggests that these objects could result from direct condensation in the solar nebula.

Our results show that the abundances of the refractory compatible elements (Sc and Yb) are fractionated from the primordial ratio (Fig. 5B). Although both refractory elements are well correlated in nonporphyritic chondrules from unequilibrated ordinary (UOC) and carbonaceous chondrites (CC), two objects from Indarch are depleted in Yb and five (out of nine) objects from Sahara 97158 have very low Sc abundances. Oldhamite, an abundant sulfide in ECs, could have acted as the carrier phase of both elements (Sc and Yb). Therefore, we suggest that formation of a sulfide, possibly oldhamite, or another reduced phase could be responsible of the observed fractionation.

The lithophile trace element abundances in Sahara 97158 and Indarch are within the range covered by nonporphyritic chondrules in UOCs (Figs. 3A and 3B), despite the different physicochemical conditions prevailing during formation of both types of chondrites. There is a tendency toward flat, CI chondrite-normalized patterns, especially for the REE except for a negative Eu anomaly. One striking difference in the abundance patterns of objects in other chondrites, like the UOC, is the negative CI chondrite-normalized Nb anomaly, which is conspicuous for many of the studied objects (Figs. 4A and 4C). Negative Eu and Yb anomalies have been reported previously for blue and red enstatite grains from unequilibrated ECs, which may be the product of either condensation or evaporation processes in the early solar nebula (Hsu and Crozaz 1998).

The two objects from Indarch in which all REE could be determined (IN4 and IN7) show relatively flat CI chondrite-normalized abundances, with no negative Eu anomaly (Fig. 3A). This REE pattern is consistent with enstatite chondrites having evolved in a reducing environment where no host phase for Eu was available during or before the formation of the objects. Their strong negative Nb anomaly correlates with a strong negative V anomaly (Fig. 7A) with some objects from Sahara 97158 falling around this trend line. All objects show a weak positive correlation between their Nb and Ti normalized abundances (Fig. 7B). These results indicate that mineral phases that incorporate V and Nb (e.g., niningerite can incorporate ~ 10 × CI Nb and Ti, Kurat et al. 2004) could have been removed from the nebular regions where these objects condensed.

In a recent study, Barrat et al. (2014) measured the abundances of some lithophile trace elements (REEs, Y, Rb, Ba, Sr, Zr, Hf, Nb, Th, U) in a suite of enstatite chondrites (EH and EL). In this study, they performed a series of leaching experiments to separate metal and sulfides in order to investigate the contributions of sulfides to the whole rock (WR) budget as well as to determine the trace element abundances of insoluble silicate fractions. The leaching procedure was able to remove nearly all sulfides and metals, leaving a residue essentially composed of silicates (e.g., enstatite and plagioclase). The results indicated that sulfides such as oldhamite are the only REE-rich phases in enstatite

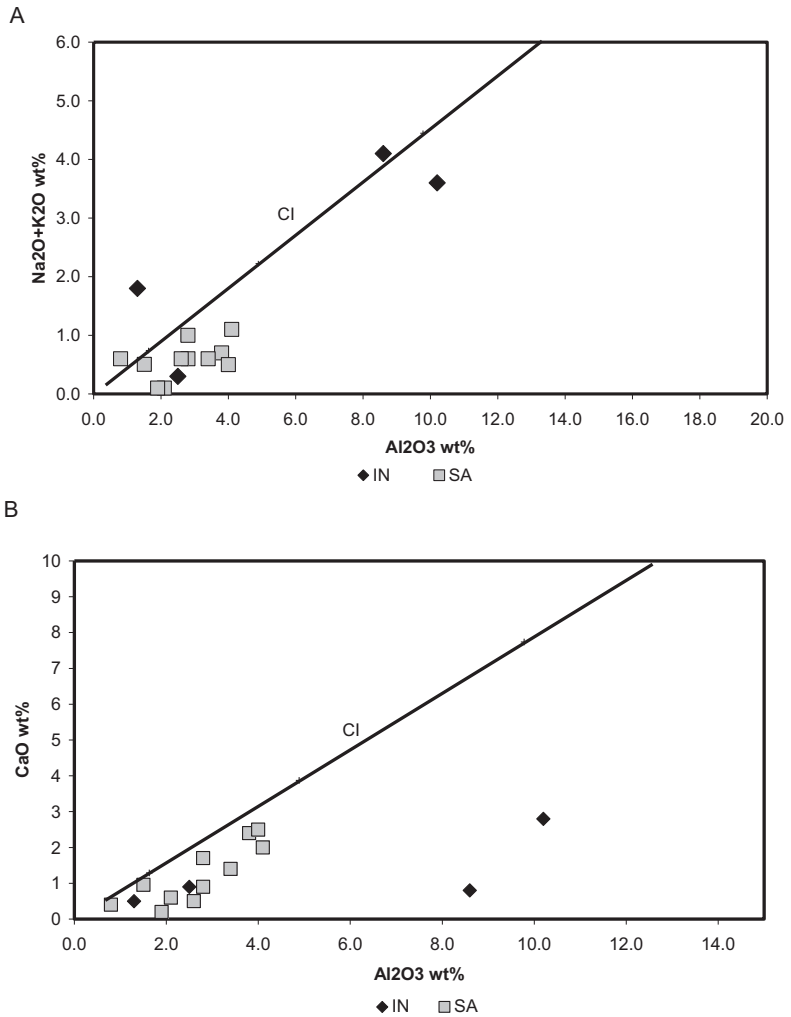

Fig. 6. A) Bulk (Na_2O+K_2O) and B) bulk CaO versus the Al_2O_3 contents compared to the respective Cl abundance ratio from Lodders and Fegley (1998).

chondrites (e.g., Crozaz and Lundberg 1995), in agreement with previous calculations for chemical equilibrium under high reducing conditions (Lodders and Fegley 1993).

Our results show that trace element contents in Indarch chondrules are variable. If the observed compositional variation is due to incorporation of variable amount of small sulfide grains in the analyzed areas, we would expect fine-grained, sulfide-rich objects to be REE enriched. The SEM images of Indarch chondrules (Figs. 2I–L) show that IN3 is very rich in fine-grained sulfides, as compared to the other studied objects. However, its trace element normalized abundances are very low, with some elements showing similar (Y, Nb, Tb, Gd, Ho, Ba) or even lower (Zr, Hf, Sr, Rb) contents, as compared to the Indarch residue (the data of Indarch residue are from Barrat et al. 2014; Fig. 8). Therefore, the compositional variability of the studied objects seems to be real rather than artifact of the microbeam measurement method.

The radiating pyroxene chondrule fragment IN6 shows refractory elements (Zr, Hf, Y) and LREE (La, Ce, Pr) concentrations with near chondritic values, with an unfractionated pattern similar to that of the Indarch whole rock (IN WR1-3, Fig. 8). Eu contents are very low (below the detection limits). In contrast HREE are fractionated relative to chondrites (Gd/Yb: ~6) with positive anomalies of Tm and Lu. The strong deficit in the LREE coupled with low Eu content could be attributed to oldhamite removal from the nebular gas prior to chondrule condensation. On the other hand, the fractionated pattern of the HREE is not what would be expected for a nebular reservoir after removal of oldhamite. Gannoun et al. (2011) reported that the oldhamite in EH3 chondrites contains Gd: ~20 × CI; Lu: ~9 × CI, with positive Yb anomaly. It is possible,

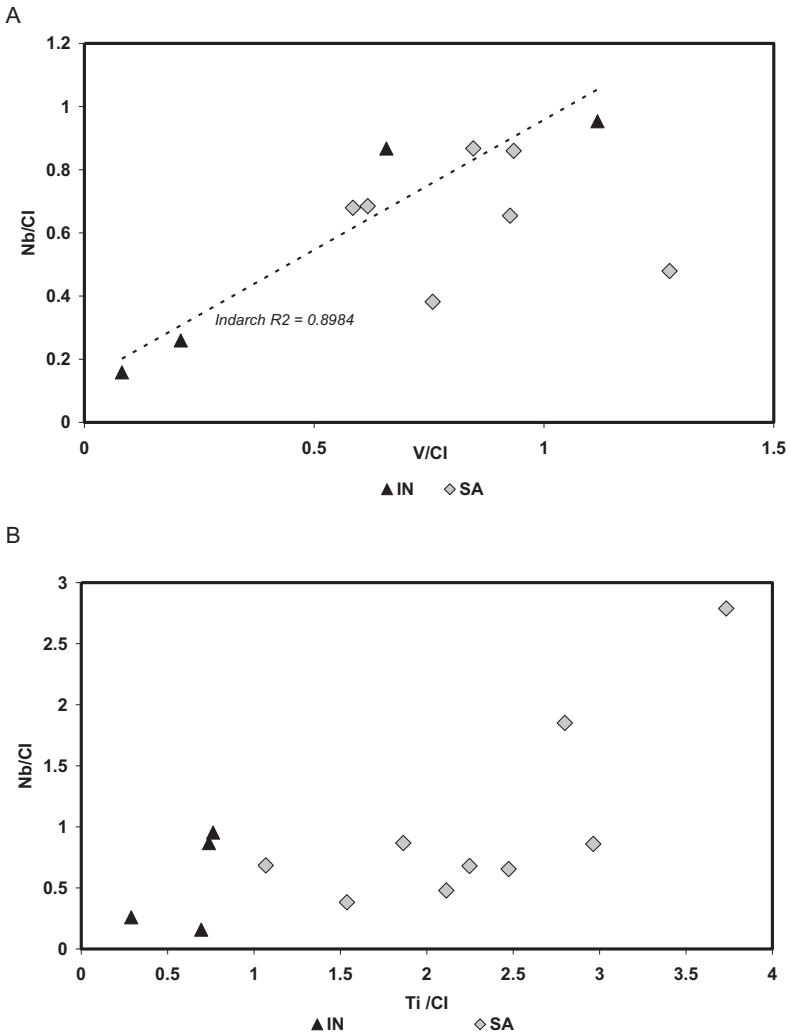

Fig. 7. Correlation plots for CI-normalized elemental abundances: A) Nb/CI versus V/CI; B) Nb/CI versus Ti/CI. The correlation line through Indarch objects ($R^2 \sim 0.9$) provides evidence for Nb-Ti fractionation.

however, that niningerite, which is present in this object, and is HREE-rich (Crozaz and Lundberg 1995; Kurat et al. 2004), controlled the bulk HREE abundances of this chondrule fragment.

All studied objects in Sahara 97158 have broadly flat, CI chondrite-normalized REE patterns with negative Eu anomalies (in objects SA7, SA9, SA12, and SA13, Eu is below the detection limits). Only SA7 shows REE abundances akin to those of the whole rock (data of whole rock Sahara 97158 are from Barrat et al. 2014), with nearly all other objects showing superchondritic REE abundances (up to $5 \times$ CI) (Fig. 9A). The high REE abundances may indicate that the chondrule analyses contain variable amounts of the REE-rich sulfide oldhamite (e.g., analysis corresponding to leached Sahara 97072 REE contents $\sim 50 \times$ CI, Fig. 9A). Although we cannot exclude that some minute sulfides could have been included, the REE contents of enstatite crystals from Sahara 97092, which may be paired with Sahara 97158 (Grossman 1998) determined by SIMS (Gannoun et al. 2011), are within the range of those present in our analyses (Fig. 9B). Only SA6 has undetectable LREE contents and shows abundances of some HREE similar to those of Sahara residue (Fig. 9A). All objects, except SA6, show very high abundances of the refractory elements Zr, Hf, Sc, and Ti. The negative Nb anomaly, which occurs as a special feature in many objects of Sahara 97158 (Fig. 4A) could be due to the removal of an Nb-enriched phase (nitride or sulfide) from the nebular gas prior to chondrule condensation. Because Nb shows a broad positive correlation with Ti (Fig. 7B), this phase could have been niningerite.

A particular feature was found in the chondrule SA10 (Fig. 4C) that gives a general idea about the time scales and/or length scales over which the postulated

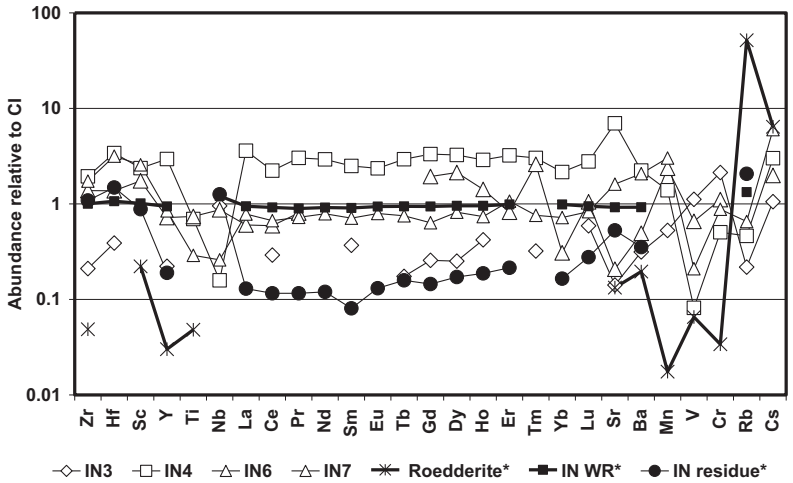

Fig. 8. Bulk analyses of lithophile trace elements normalized to Cl chondrite abundances of objects from Indarch, compared to those of Indarch whole rock (IN WR), Indarch residue (IN residue) (both from Barrat et al. 2014) and roedderite (from Hsu 1998).

nebular removal processes took place. SA10 is a layered chondrule in which the olivine-rich core is strongly depleted in Nb as compared to its pyroxene-rich rim, which shows only a slight Nb depletion. Removal of a Nb-rich phase from the nebular gas must have occurred on the time scales and/or over length scales of formation of an individual chondrule in order to explain the core-rim contrasts in Nb concentration preserved in this object.

The Moderately and Strongly Volatile Elements

Moderately and strongly volatile elements are "irregularly fractionated." By this term, we mean that fractionation is not a function of condensation temperature, volatility, or mineral partitioning and therefore, is not a smooth function of cosmochemical or geochemical properties of the elements. A typical example, as found previously in UOCs (Engler et al. 2007), is when moderately volatile elements are depleted but strongly volatile elements are not. It takes at least two steps to create this fractionation.

The more refractory of the moderately volatile elements (Sr and Ba) are enriched and depleted in objects from both Sahara 97158 and Indarch enstatite chondrites (Figs. 3 and 4). The negative abundance anomalies of Sr and Ba in studied objects are interpreted as the result of vapor fractionation, because Sr and Ba are more volatile than elements between Zr and Lu.

Enrichments of Sr and Ba may have different causes. In objects of Sahara 97158, the Sr and Ba enrichments are coupled with high contents in Rb, U, and Th (Fig. 10). Because all of these elements are very abundant in the terrestrial crust, such enrichments may be explained by terrestrial contamination, most likely where Sahara 97158 fell in the desert. The fine-grained rim from SA10 object is enriched in Sr and Ba relative to its core (Fig. 4C), supporting this view. Object IN7 from Indarch, follow the Sr, Ba, and Rb trends of Sahara 97158 chondrules (Fig. 10) and may have the same explanation of terrestrial contamination. However, in other objects, such as IN4, the origin of the enrichments in Sr and Ba are not clear. At first sight, the enrichments could be a consequence of the microbeam analyses including disproportionately high abundances of plagioclase ($D_{Sr\ Plag/liq} = 1.55$; Bindeman et al. 1998) in the analyzed areas, consistent with the high Al_2O_3 contents (Table 4). But this seems not to be the case because the REEs are not fractionated and instead display a flat, CI chondrite-normalized abundance pattern.

The moderately volatile elements V, Cr, and Mn have similar behavior especially in objects of the Sahara 97158 chondrite. These elements are olivine/pyroxene compatible and could have been added to the objects by equilibration with the chondritic reservoir. Because these elements are easily accommodated in pyroxene-dominated chondrules, they are present in slightly superchondritic amounts. In Indarch, the variation in Mn contents could be related to possible contamination with sulfides. The three objects, IN4, IN6, and IN7, showing high abundances of Mn (1.4–3 × CI; Fig. 8) are also those in which the sulfide niningerite was detected (Table 2). Troilite and oldhamite are the main sulfides present in IN3 (Mn ~ 0.5 × CI).

In Sahara 97158, the normalized abundances of the moderately volatile to strongly volatile elements (V to Cs) increase with decreasing condensation temperature. The moderately volatiles Rb and Cs have abundances similar to those of the REE (~2 × CI), with exception of SA1, with some objects being enriched in Rb as compared to the whole rock and residue (Fig. 9A). These patterns

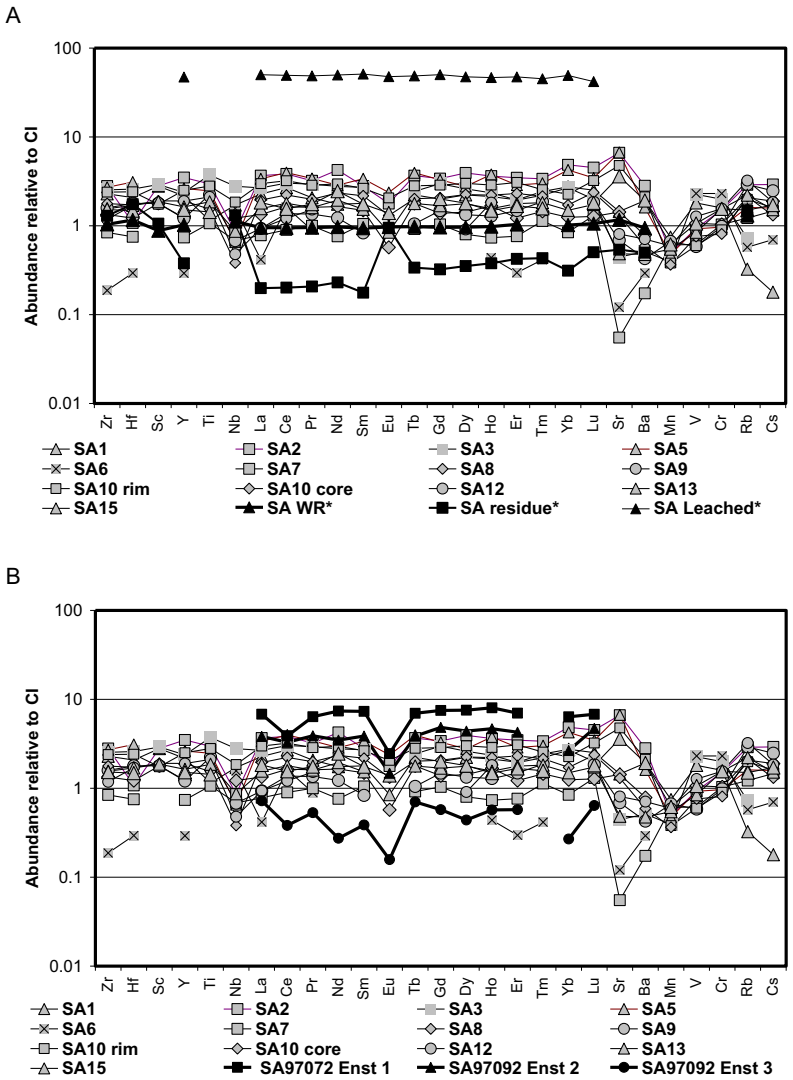

Fig. 9. A) Bulk analyses of lithophile trace elements normalized to Cl chondrite abundances of objects from Sahara 97158. Data of whole rock and residue from Sahara 97158 (SA WR and SA residue) and leached Sahara 97072 (SA Leached) are from Barrat et al. (2014). B) SIMS analysis of Sahara 97092 (which is possibly paired with Sahara 97158) enstatite (SA97092 Enst 1-Enst 3) from Gannoun et al. (2011).

suggest that these elements were probably added to the objects by metasomatic processes. In this case, the pyroxene-compatible transition elements were acquired during equilibration with the chondritic reservoir (e.g., V, Cr), whereas Rb and Cs, present in superchondritic amounts and unfractionated relative abundances, were added to the objects while they remained in contact with the cooling volatile-rich vapor. However, this process did not run to completion in all objects. The SA1 chondrule appears to have escaped such an event. An early separation of the object from the vapor may have prevented the full acquisition of the volatile elements Rb and Cs (Fig. 4B).

The volatile element abundances in objects of Indarch are quite peculiar. All objects are enriched in Cs but depleted in Rb. The latter show abundances lower than those of the whole rock and residue, which is mainly composed of silicates (Fig. 8). The fact that Rb is depleted in chondrules and chondrule fragments in Indarch as compared to similar objects from Sahara 97158 may indicate that a distinct event affected the Indarch chondrules. However, if such an event took place in the nebular gas, both elements (Rb and Cs) should be equally depleted, as they have similar condensation temperatures (50% condensation temperature ~800 K; Lodders 2003). Therefore, the Rb-Cs fractionation in chondrules of Indarch suggests that these objects were disturbed during a later metasomatic process.

We suggest that a postaccretion process such as diffusion preferentially mobilized Rb (atomic radius:

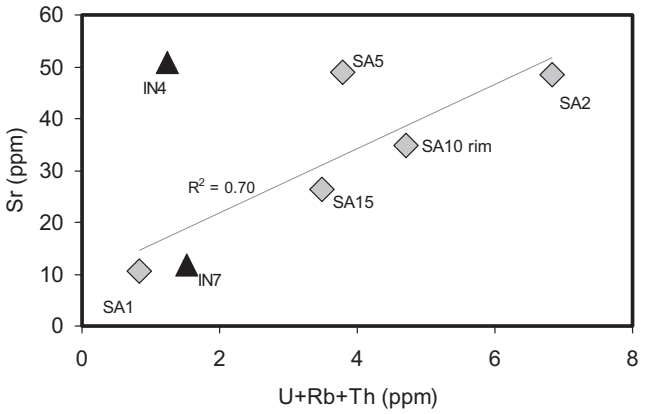

Fig. 10. Element correlation plots for Sr versus U + Th + Rb concentrations of the studied objects from Sahara 97158 (SA) and Indarch (IN). The correlation line through Sahara objects ($R^2 \sim 0.7$) is consistent with terrestrial contamination.

1.48 Å) with respect to Cs (atomic radius: 1.69 Å) into a Na+K-bearing phase forming part of the matrix, producing the low Rb contents of the studied chondrules. One such mineral may be roedderite ($[Na, K]_2[Mg, Fe]_5[Si, Al]_{12}O_{30}$), which has been identified previously in the Indarch chondrite (Fuchs et al. 1966). Trace elements contents of roedderite demonstrate enrichments in alkali elements (e.g., Rb ~ 50 × CI) and depletions in siderophile and refractory lithophile elements (Hsu 1998) (Fig. 8). Roedderite occurs in the matrix of unequilibrated enstatite chondrites as euhedral crystals (Hsu 1998) and is associated with sphalerite in Indarch (El Goresy and Ehlers 1989). In addition, it has been identified in other unequilibrated EH chondrites (Keil 1968; Rambaldi et al. 1986; Kimura and El Goresy 1988; El Goresy and Ehlers 1989) and in the aubrite Bustee (Hsu 1998). It is unclear if roedderite condensed in the same region of the solar nebula as the ECs or was transported from another more oxidizing environment of the nebula (El Goresy and Ehlers 1989). Accordingly, the occurrence of roedderite embedded inside sulfide minerals like niningerite in the matrix is an example of nonequilibrium accretion. However, its textural occurrence in the EH3 Qingzhen led Rambaldi et al. (1986) to suggest that it might represent the precipitate of an alkali-rich fluid phase, possibly developed during planetary processes in the enstatite chondrite parent body.

Although the constituents of the matrix in enstatite chondrites, as well as the relationship of matrix from one chondrite group to another is far from completely understood (e.g., Kimura 1988; Weisberg and Kimura 2012; Weisberg et al., 2014), the presence of roedderite in Indarch seems to have played a key role in the volatile element distribution in Indarch chondrules. Enstatite chondrites show highly heterogeneous volatile element abundances with the EH type showing the highest abundances (Hertogen et al. 1983). Our results lead us to suggest that the high abundance of volatile elements in the studied objects may have its roots in a metasomatic event that did not run to completion. The geochemical record of such a process remained undisturbed in many objects of EH3 Sahara 97158 but was partially modified in those from EH4 Indarch.

CONCLUSIONS

Petrographic and chemical study of individual nonporphyritic chondrules and chondrule fragments in the Sahara 97158 (EH3) and Indarch (EH4) chondrites shows that each object may reflect a complex and unique history. Notwithstanding these unique features, Sahara 97158 and Indarch chondrules show a common elemental feature, negative Nb and Eu anomalies, which are conspicuous for many objects of the studied ECs.

Unfractionated, solar-like ratios for elements with different geochemical behavior (e.g., Yb/Ce ratios and CI chondrite-normalized REE abundance patterns) shows that many primordial elemental ratios of these objects were not modified during postaccretion processing, and therefore, point toward the predominance of cosmochemical processes (condensation) during chondrule formation. Negative abundance anomalies for medium volatile elements (Sr and Ba) in the studied objects are interpreted as the result of fractionation processes in the solar gas where ECs condensed.

A distinct fractionation mechanism, possibly unique for ECs, was apparently active during chondrule formation. Subchondritic CaO/Al_2O_3 ratios; nonchondritic Yb/Sc ratios; and deficits in chondritic-normalized Nb, Ti, V, and Mn abundances in the studied objects reflect element partitioning by sulfide or other reduced phase such as oldhamite or niningerite in the solar gas. Removal of elements from the solar gas by this phase occurred over the time scales and/or over the length scales of the formation of an individual chondrule and so could be recorded during nebular accretion of a single object.

Normalized abundances of moderately volatile and volatile elements in Sahara 97158 increase with decreasing condensation temperatures indicating that these elements could have been added during a late nebular event. Continued interaction of the pyroxene-rich objects with the cooling nebular gas would promote a variety of elemental exchanges. In this way, moderately volatile as well as strongly volatile elements could have been added to the objects. In objects from equilibrated Indarch EH4, Rb is depleted with respect to Cs. Because this fractionation cannot be attributed to a late nebular event, we suggest that a postaccretion process such as diffusion preferentially mobilized Rb

with respect to Cs into a Na+K-bearing phase such as roedderite that forms part of the matrix. Our results lead us to suggest that the chaotic behavior of the moderately and strongly volatile elements is likely due to variations in the efficiency of a metasomatic event. The elemental record of such a process remained undisturbed in many objects of EH3 Sahara 97158, but was partially modified in those from EH4 Indarch.

Acknowledgments—We thank the late Dr. Gero Kurat for his constructive discussions, encouragement, and support through the years. The manuscript benefited from the comments of M. Weisberg and an anonymous reviewer. Financial support was received from NSERC Discovery Grant Program (PJS) and CONICET (PIP 063), Agencia (PICT 0142), Argentina. A. Engler received a visiting PhD research scholarship award from Memorial University.

Editorial Handling—Dr. A. J. Timothy Jull

REFERENCES

Anders E. 1964. Origin, age, and composition of meteorites. *Space Science Reviews* 3:583–714.

Barrat J. A., Zanda B., Jambon A., and Bollinger C. 2014. The lithophile trace elements in enstatite chondrites. *Geochimica et Cosmochimica Acta* 128:71–94.

Berlin J., Jones R. H., Brearley A. J., and Spilde M. N. 2008. Determining bulk chemical compositions of chondrules by electron microprobe: Modal recombination versus defocused beam analyses. *Microscopy and Microanalysis* 14:110–111.

Bindeman I. N., Davis A. M., and Drake M. J. 1998. Ion microprobe study of plagioclase-basalt partition experiments at natural concentration levels of trace elements. *Geochimica et Cosmochimica Acta* 62:1174–1193.

Blander M., Pelton A. D., and Jung I. H. 2009. A condensation model for the formation of chondrules in enstatite chondrites. *Meteoritics & Planetary Science* 44:531–543.

Clayton R. N. and Mayeda T. K. 1984. Oxygen isotopic compositions of enstatite chondrites and aubrites. *Journal of Geophysics Resources* 89:C245–C249.

Crozaz G. and Lundberg L. L. 1995. The origin of oldhamite in unequilibrated enstatite chondrites. *Geochimica et Cosmochimica Acta* 59:3817–3831.

Ebel D. S. and Alexander C. M. O'D. 2011. Equilibrium condensation from chondritic porous IDP enriched vapor: Implications for Mercury and enstatite chondrite origins. *Planetary Space Science* 59:1888–1894.

Ebihara M. 1988. Trace element composition and distribution of Yamato-691: An equilibrated enstatite chondrite. *Proceedings of the NIPR Symposium Antarctic Meteorites* 1:102–112.

El Goresy A. and Ehlers K. 1989. Sphalerite in EH chondrites: I textural relations, compositions, diffusion profiles and pressure temperature histories. *Geochimica et Cosmochimica Acta* 53:1657–1668.

Engler A., Kurat G., and Sylvester P. J. 2003. A chemical and petrological study of chondrules and micro-objects in some CM2, CR2 and C3 chondrites (abstract #5157). *Meteoritics & Planetary Science* 38:A86.

Engler A., Varela M. E., Kurat G., Ebel D., and Sylvester P. J. 2007. The origin of non-porphyritic pyroxene chondrules in UOCs: Liquid solar nebula condensates? *Icarus* 192:248–286.

Fitoussi C. and Bourdon B. 2012. Silicon isotope evidence against an enstatite chondrite earth. *Science* 335:1477–1480.

Fleet M. E. and MacRae N. D. 1987. Sulfidation of Mg-rich olivine and the stability of niningerite in enstatite chondrites. *Geochimica et Cosmochimica Acta* 51:1511–1521.

Frazier R. M. and Boynton W. V. 1985. Rare earth and other elements in components of the Abee enstatite chondrite. *Meteoritics* 20:197–218.

Fuchs L. H., Frondel C., and Klein C. 1966. Roedderite, a new mineral from the Indarch meteorite. *American Mineralogist* 51:949–955.

Gannoun A., Boyet M., El Goresy A., and Devouard B. 2011. REE and actinide microdistribution in Sahara 97072 and ALHA77295 EH3 chondrites: A combined cosmochemical and petrologic investigation. *Geochimica et Cosmochimica Acta* 75:3269–3289.

Gooding J. L. and Keil K. 1981. Relative abundances of chondrule primary textural types in ordinary chondrites and their bearing on conditions of chondrule formation. *Meteoritics* 16:17–43.

Grossman J. N. 1998. The Meteoritical Bulletin, No. 82. *Meteoritics & Planetary Science* 33:221–239.

Grossman J. N., Rubin A. E., Rambaldi E. R., Rajan R. S., and Wasson J. T. 1985. Chondrules in the Qingzhen type-3 enstatite chondrite: Possible precursor components and comparison to ordinary chondrite chondrules. *Geochimica et Cosmochimica Acta* 49:1781–1795.

Grossman J. N., Alexander C. M. O'D., Wang J., and Brearley A. 2002. Zoned chondrules in Semarkona: Evidence for high- and low-temperature processing. *Meteoritics & Planetary Science* 37:49–73.

Hertogen J., Janssens M.-J., Takahashi H., Morgan J. W., and Anders E. 1983. Enstatite chondrites—Trace element clues to their origin. *Geochimica et Cosmochimica Acta* 47:2241–2255.

Hsu W. 1998. Geochemical and petrographic studies of oldhamite, diopside, and roedderite in enstatite meteorites. *Meteoritics & Planetary Science* 33:291–301.

Hsu W. and Crozaz G. 1998. Mineral chemistry and the origin of enstatite in unequilibrated enstatite chondrites. *Geochimica et Cosmochimica Acta* 62:1993–2004.

Jackson S. 2001. The application of Nd:YAG lasers in LA-ICP-MS. In *Laser Ablation-ICPMS in the earth sciences, principles and application*, edited by Sylvester P. *Mineralogical Association of Canada* 29:29–45.

Jackson S., Longerich H. P., Dunning G. R., and Fryer B. J. 1992. The application of laser-ablation microprobe-inductively coupled plasma—mass spectrometry (LAM-ICP-MS) to in situ trace-element determinations in minerals. *Canadian Mineralogist* 30:1049–1064.

Jenner G. A., Foley S. F., Jackson S. E., Green T. H., Fryer B. J., and Longerich H. P. 1993. Determination of partition coefficients for trace elements in high pressure–temperature experimental run products by laser ablation microprobe-inductively coupled plasma-mass spectrometry (LAM-ICPMS). *Geochimica et Cosmochimica Acta* 58:5099–5103.

Kallemeyn G. W. and Wasson J. 1986. Compositions of enstatite (EH3, EH4,5 and EL6) chondrites: Implications

regarding their formation. *Geochimica et Cosmochimica Acta* 50:2153–2164.
Keil K. 1968. Mineralogical and chemical relationships among enstatite chondrites. *Journal of Geophysics Resources* 73:6945–6976.
Keil K. 1984. Enstatite meteorites and their parent bodies. *Meteoritics* 24:195–208.
Kimura M. 1988. Origin of opaque minerals in an unequilibrated enstatite chondrite Yamato-691. In *Proceedings of the NIPR Symposium on Antarctic Meteorites*, vol. 1. Tokyo: National Institute of Polar Research. pp. 51–64.
Kimura M. and El Goresy A. 1988. Djerfisherite compositions in EH chondrites: A potential parameter to the geochemistry of the alkali elements (abstract). *Meteoritics* 23:279–280.
Kimura M. and Lin Y. 1999. Petrological and mineralogical study of enstatite chondrites with reference to their thermal histories. *Antarctic Meteorites Resources* 12:1–18.
Kurat G. 1988. Primitive meteorites: An attempt towards unification. *Philosophical Transactions of the Royal Society of London Series A* 325:459–482.
Kurat G., Zinner E., Brandstätter F., and Ivanov V. 2004. Enstatite aggregates with niningerite, heideite, and oldhamite from the Kaidun carbonaceous chondrite: Relatives of aubrites and EH chondrites? *Meteoritics & Planetary Science* 39:53–60.
Larimer J. W. 1968. An experimental investigation of oldhamite CaS; and the petrological significance of oldhamites in meteorites. *Geochimica et Cosmochimica Acta* 32:965–982.
Larimer J. W. and Ganapathy R. 1987. The trace element chemistry of CaS in enstatite chondrites and some implication regarding its origin. *Earth and Planetary Science Letters* 84:123–134.
Lehner S. W., Buseck P. R., and McDonough W. F. 2010. Origin of kamacite, schreibersite, and perryite in metal-sulfide nodules of the enstatite chondrite Sahara 97072 (EH3). *Meteoritics & Planetary Science* 45:289–303.
Lehner S. W., Petaev M. I., Zolotov M. Y., and Buseck P. R. 2013. Formation of niningerite by silicate sulfidation in EH3 enstatite chondrites. *Geochimica et Cosmochimica Acta* 101:34–56.
Lin Y. and El Goresy A. 2002. A comparative study of opaque phases in Qingzhen (EH3) and MAC 88136 (EL3): Representatives of EH and EL parent bodies. *Meteoritics & Planetary Science* 37:577–600.
Lodders K. 2003. Solar system abundances and condensation temperatures of the elements. *The Astrophysical Journal* 591:1220–1247.
Lodders K. and Fegley B. Jr. 1993. Lanthanide and actinide chemistry at high C/O ratios in the solar nebula. *Earth and Planetary Science Letters* 117:125–145.
Lodders K. and Fegley B. 1998. *The planetary scientist companion*. New York: Oxford University Press. 371 p.
Lundberg L. L. and Crozaz G. 1988. Enstatite chondrites: A preliminary ion microprobe study (abstract). *Meteoritics* 23:285.
Lusby D., Scott E. R. D., and Keil K. 1987. Ubiquitous high FeO silicates in enstatite chondrites. Proceedings, 17th Lunar and Planetary Science Conference. pp. E679–E695.
McCoy T., Dickinson T. L., and Lofgren G. E. 1999. Partial melting of the Indarch (EH4) meteorite: A textural, chemical, and phase relations view of melting and melt migration. *Meteoritics & Planetary Science* 34:735–746.
Paniello R. C., Day J. M. D., and Moynier F. 2012. Zinc isotopic evidence for the origin of the Moon. *Nature* 490:376–379.
Petaev M. I., Lehner S. W., and Buseck P. R. 2011. Processing of silicates in S-rich systems: Implications for the origin of enstatite chondrites. Workshop on Formation of the First Solids in the Solar System, held November 7–9, 2011 in Kauai, Hawaii. LPI Contribution 1639. 9095 p.
Rambaldi E. R., Rajan R. S., Wang D., and Housley R. M. 1983. Evidence for relict grains in chondrules of Qingzhen, an E3 type enstatite chondrite. *Earth and Planetary Science Letters* 66:11–24.
Rambaldi E. R., Rajan R. S., and Housley R. M. 1986. Roedderite in the Qingzhen (EH3) chondrite. *Meteoritics* 21:141–149.
Rubin A. E. and Grossman J. N. 1987. Size-frequency-distributions of EH3 chondrules. *Meteoritics* 22:238–251.
Rubin A. E., Scott E. R. D., and Keil K. 1997. Shock metamorphism of enstatite chondrites. *Geochimica et Cosmochimica Acta* 61:847–858.
Savage P. S. and Moynier F. 2013. Silicon isotopic variation in enstatite meteorites: Clues to their origin and Earth-forming material. *Earth and Planetary Science Letters* 361:487–496.
Sears D. W. G., Kalemeyn G. W., and Wasson J. T. 1982. The compositional classification of chondrites. II. The enstatite chondrites. *Geochimica et Cosmochimica Acta* 46:597–608.
Sears D. W., Kallemeyn G. W., and Wasson J. T. 1983. Composition and origin of clast and inclusions in the Abee enstatite chondrite breccia. *Earth and Planetary Science Letters* 62:180–192.
Varela M. E., and Kurat G. 2009. Glasses in meteorites and the primary liquid condensation model. *Mitteilungen der Österreichischen Mineralogischen Gesellschaft* 155:279–320.
Varela M. E., Sylvester P., Brandstätter F., and Engler A. 2014. Non-porphyritic chondrules in enstatite chondrites (abstract #5259). *Meteoritics & Planetary Science* 49:LPI Contribution No. 1800, id.5259.
Warren P. H. 1997. The unequal host-phase density effect in electron probe defocused beam analysis: An easily correctable problem (abstract #1406). 28th Lunar and Planetary Science Conference. CD-ROM.
Warren P. 2011. Stable-isotopic anomalies and the accretionary assemblage of the Earth and Mars: A subordinate role for carbonaceous chondrites. *Earth and Planetary Science Letters* 311:93–100.
Weisberg M. K. and Kimura M. 2012. The unequilibrated enstatite chondrites. *Chemie der Erde* 72:101–115.
Weisberg M. K., Prinz M., and Fogel R. A. 1994. The evolution of enstatite and chondrules in unequilibrated enstatite chondrites: Evidence from iron-rich pyroxene. *Meteoritics* 29:362–373.
Weisberg M. K., Connolly H. Jr., Ebel D. S., and Kimura M. 2006. Sulfide-metal nodules in EH3 chondrites (abstract #5317). *Meteoritics & Planetary Science* 41:A186.
Weisberg M. K., Zolensky M. E., Kimura M., and Ebel D. S. 2014. Primitive fine-grained matrix in the unequilibrated enstatite chondrites (abstract #1551). 45th Lunar and Planetary Science Conference. CD-ROM.